THE JOURNAL OF PHYSICAL CHEMISTRY C
A JOURNAL OF THE AMERICAN CHEMICAL SOCIETY

pubs.acs.org/JPCC

Article

Polarized Hole Injection-induced Magnetic Enhancement in Carbon-Encapsulated Cobalt Ferrite Nanoparticles

Jiann-Shing Lee, Shih-Min Hung, Chun-Rong Lin, Chi-Liang Chen, Jau-Wern Chiou, Chih-Yu Hua, Huang-Ming Tsai, Way-Faung Pong, Chien-Te Chen, Wen-Bin Wu,* and Jiunn Chen*

Cite This: J. Phys. Chem. C 2023, 127, 17978−17986

ABSTRACT: Magnetic enhancement was observed in carbon-encapsulated cobalt ferrite ($CoFe_2O_4$) nanoparticles. The induced magnetic moment of the nanoparticles was estimated using a vibrating-sample magnetometer and corrected based on thermogravimetric loss. Notably, up to 25% magnetic enhancement was achieved via carbon encapsulation by low-temperature hydrothermal reactions. A systematic variation on Co L-edge absorption spectra revealed the introduction of valence holes owing to carbon encapsulation, and the hole injection was attributed to carbon−sp contact. X-ray magnetic circular dichroism indicates holes injected upon both Fe and Co ions. Specifically, it is observed that the injection of polarized holes into Co^{2+} ions at the octahedral site results in magnetic enhancement. A spin−split electronic structure analysis of $CoFe_2O_4$ based on density functional theory with Hubbard correction demonstrated that octahedral Co, which served as a minority hole reservoir, controlled the magnetic properties of the hybrid system.

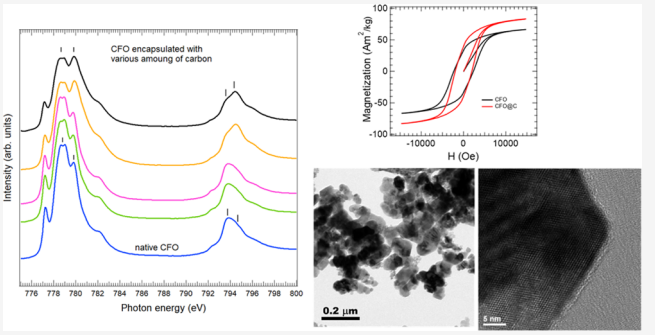

1. INTRODUCTION

The applications of magnetic nanomaterials in magnetic recording media,[1,2] micromagnetic devices, magnetoelectric materials,[3,4] microwave absorption applications,[5−7] biosensors,[8] medical diagnostics, and therapy[9−11] have been comprehensively studied for decades. Spinel ferrites, a class of metal oxides with extraordinary physical properties, are the most extensively studied ferrimagnetic materials.[12,13] High-magnetization materials are particularly desirable for the development of advanced multifunctional magnetic applications. Unfortunately, a significant reduction in magnetization occurs at the surface of spinel ferrite nanoparticles (NPs), rendering them less useful for many of these applications. However, this obstacle can be overcome by coating the magnetic NPs with various polymers and organic acids.[14−16]

Amorphous carbon (a-C) is a low-cost, environmentally friendly, and chemically stable coating material. Carbon coating is not widely reported because the formation of carbon shells usually needs a high-temperature annealing process, which carbonizes hydrocarbon precursors but will also result in the reduction.[17] A method to avoid this is to use presynthesized magnetic NPs and low-temperature heat treatment. Recently, Lee et al.[18,19] reported ferrimagnetic enhancement in a hybridized system of a-C-encapsulated magnetite nanoparticles (Fe_3O_4@a-C NPs). Carbon encapsulation enhanced the magnetization of the Fe_3O_4 NPs by approximately 22.5%, drawing renewed attention to intriguing insights into promoting magnetism. Lee et al. demonstrated that when Fe_3O_4 NPs are brought in contact with a metal-like electrode material (a-C), the Fermi level of the electrode material is pinned to the conduction band minimum of the magnetic semiconductor and becomes spin-dependent. A later work,[19] based on synchrotron spectroscopy, confirmed the polarized electron injection manifests a chemical reduction of tetrahedral Fe^{3+} as the root cause for the observed room temperature magnetic enhancement in Fe_3O_4@a-C NPs.

As an extension of understanding the magnetic characteristics of spinel ferrite NPs with a-C encapsulation, in this study, we synthesized carbon-encapsulated cobalt ferrite $CoFe_2O_4$ (CFO) by the hydrothermal reaction. The crystal structure of CFO is identical to Fe_3O_4 but Co substitutes for one of the Fe ions at the octahedral sublattice in an ideal inverse spinel. CFO can be symbolized as $[Fe^{3+}]_{tet\downarrow}[Co^{2+}Fe^{3+}]_{oct\uparrow}O_4$, where the subscript tet (oct) denotes the tetrahedral (octahedral) sublattice.[20] The magnetic moments of ions in each site are oppositely oriented, forming a ferrimagnetic configuration. A simple ionic picture yields high-spin configuration $t_{2g}^{3\uparrow}e_g^{2\uparrow}t_{2g}^{2\downarrow}$ ($t_{2g}^{3\uparrow}$

Received: May 8, 2023
Revised: August 16, 2023
Published: August 29, 2023

$e_g^{2\uparrow}$) for Co^{2+} (Fe^{3+}) in the octahedral sublattice; $e^{2\downarrow}t_2^{3\downarrow}$ for Fe^{3+} in the tetrahedral sublattice. Here, the notations ↑ and ↓ denote spin direction parallel and antiparallel to total magnetization. We denote spin-majority (-minority) ↑ (↓) throughout the manuscript. Magnetic moments of Fe^{3+} ions in each sublattice are canceled, and thus, $3\mu_b$ per $CoFe_2O_4$ formula are determined based on the simplified high-spin Co^{2+} ionic scheme. Based on material preparation and purity, the magnetization of CFO nanoparticle samples at room temperature with maximum applied field ($M_{max.}$) up to 15 kOe can reach about 79 emu/g.[21,22] The $M_{max.}$ was smaller than those for the bulk material (89 emu/g)[23] and single crystal (84 emu/g)[24] under the same applied field.

Among spinel ferrites, nanosized CFO is highly promising in terms of imparting specific properties. This is owing to its high coercivity, strong crystalline anisotropy, moderate magnetization, high Curie temperature (520 °C), and high chemical and thermal stability. In the present study, up to 25% magnetic enhancement was achieved via an a-C encapsulation. Interestingly, in contrast to promoting magnetism by the polarized electron injection in Fe_3O_4@a-C, the polarized hole injection engendered the magnetic enhancement in CFO@C was uncovered by soft X-ray spectroscopy. In addition, first-principles calculations revealed that octahedral Co of minority spin in the vicinity of E_F served as hole reservoirs, controlling the magnetic enhancement in the hybrid system.

2. METHODS

2.1. Sample Preparations. CFO NPs used in this work were obtained from US Research Nanomaterials, Inc. (Houston, Texas). Starch is an ideal coating precursor because of the abundant availability, low cost, renewability, biocompatibility, biodegradability, and nontoxicity.[25] Hence, a low-temperature annealing method to prepare carbon-coated CFO NPs by using starch as the carbon precursor was followed in this work.[26] To form CFO@a-C samples, 0.02, 0.05, 0.1, and 0.2 g of the starch are dissolved in 100 mL of deionized water containing 0.5 g of CFO NPs, and the corresponding samples are referred to as CFO@0.02C, CFO@0.05C, CFO@0.1C, and CFO@0.2C, respectively, in this paper. After ultrasonic treatment for another 15 min, the resulting suspensions were transferred to the autoclave, and the low-temperature hydrothermal reactions were performed at 200 °C for 12 h. After completion of the reaction, the autoclave was cooled to room temperature, and the resulting CFO@a-C NPs were collected using a magnet and washed six times with deionized water. The final product was oven-dried at 60 °C for 12 h.

2.2. Experimental Setup. XRD patterns were acquired to reveal crystalline phases of $CoFe_2O_4$ and $CoFe_2O_4$@a-C samples by using a Bruker D8 Advanced eco (Billerica, Massachusetts) with a Cu Kα radiation source. The scanning condition for this analysis was an angular range of 10−80° (2θ), with a 0.02° step size, and the data collection rate was 4s per step. These samples were characterized by a high-resolution transmission electron microscope (HRTEM, JEOL JEM-2100F/Cs STEM) to inspect their size and the thickness of the carbon layer. For HRTEM, samples were prepared by placing one drop of a dilute particle suspension in anhydrous alcohol on a carbon-coated copper grid and evaporating the solvent at room temperature. Their Raman spectra were collected at random points under a 20× objective using a microscopic Raman system (RAMaker, Protrustech Co., Ltd., Taiwan). An exciting line of 532 nm was supplied by a diode laser (CNI) with a power of 1 mW. The scanned spectral range was 200−1800 cm^{-1} with a spectral resolution of 1 cm^{-1}, and the exposure time was 60s, with two accumulations. Thermogravimetric analysis (TGA) of these test samples was done using an SDT Q600 instrument from TA Instruments. The temperature ranged from 45 to 800 °C, and the heating rate of TGA curves was 10 °C/min using a purge gas flow rate of 100 mL/min argon atmosphere for the evaluation of the mass fraction of the particles. In addition, a vibrating-sample magnetometer (VSM, Lake Shore 7400 system) was used to observe induced magnetization and M−H loop measurements under the magnetic field (H) up to 15 000 Oe. The soft X-ray experiments were performed at the TPS 45A2 beamline[27,28] of the National Synchrotron Radiation Research Center in Taiwan. The total electron yield method was used to measure the X-ray absorption and the X-ray magnetic circular dichroism across the Co and Fe L-edge, with left- and right-handed circularly polarized light along with an applied magnetic field of 1.5 T.

3. RESULTS

3.1. Crystal Structure. Figure 1 shows the X-ray diffraction patterns of the CFO and CFO@0.2C samples.

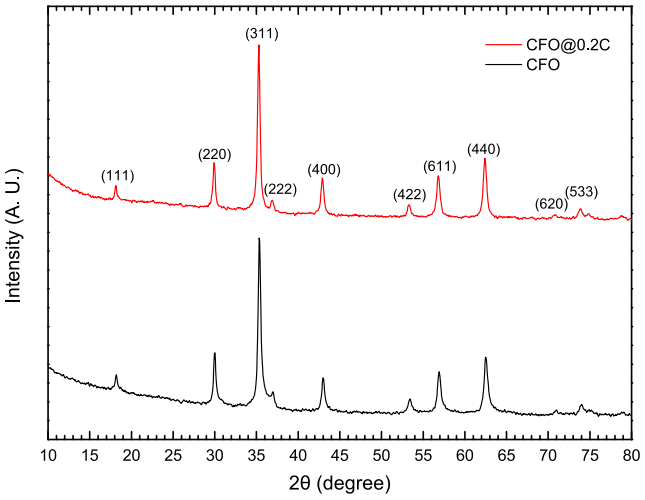

Figure 1. X-ray diffraction patterns of CFO and CFO@0.2C samples.

The acquired $CoFe_2O_4$@0.2C sample exhibited a similar XRD pattern as the $CoFe_2O_4$, suggesting the crystalline form was nearly unchanged during the hydrothermal process. All of the diffraction peaks could be indexed to an inverse spinel structure of $CoFe_2O_4$ (JCPDS no. 22-1086). No additional crystalline phase apart from CFO after hydrothermal treatment was detected for CFO@0.2C NPs. Crystal structures of these two samples in space group $Fd\bar{3}m$ have been refined by application of the Rietveld method X-ray powder diffraction profile. Refinements were carried out using GSAS software and EXPGUI interface. The average crystalline sizes calculated from the refined profile parameter were determined to be 23.1 nm (CFO) and 24.0 nm (CFO@0.2C), respectively. The CFO and CFO@C NPs are nearly granular in shape as determined by TEM, as seen in Figure 2a. The HRTEM images revealed a noticeably dark core and gray carbon shell in the encapsulated CFO@a-C NPs. Shell thickness less than the information depth of soft X-ray was ensured and was roughly proportional to the amount of starch used. The XRD and HRTEM results

https://doi.org/10.1021/acs.jpcc.3c03046
J. Phys. Chem. C 2023, 127, 17978−17986

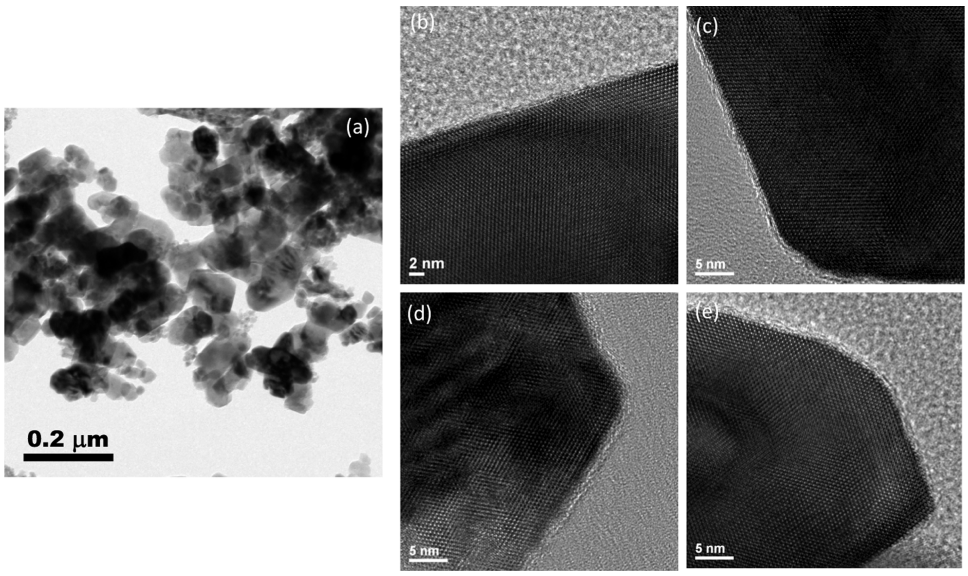

Figure 2. (a) Representative TEM micrograph of CFO@a-C nanoparticles. HRTEM images of a single CFO@C nanoparticle of samples (b) CFO@0.02C, (c) CFO@0.05C, (d) CFO@0.1C, and (e) CFO@0.2C.

demonstrate a well-defined core−shell structure, and the CFO crystalline phase is unaffected by carbon encapsulation.

3.2. Raman Analysis. Figure 3 shows the Raman spectra of all of the test samples in the low- and high-wavenumber regions. The characteristic Raman vibration modes of the spinel crystalline structure are present for these samples, although slightly red-shifted compared to thin CFO films.[29−31] However, a much lower signal/noise ratio of their vibration modes can be easily found for CFO@C composites, caused by carbon coating. All Raman bands of CFO@a-C exhibited a typical spectrum of diamond-like carbon, suggesting that the starch was converted into a carbon-like product at 200 °C in the hydrothermal carbonization process. This band region could be deconvoluted into a broad band at 1330−1350 cm^{-1} (D band) and another band at 1540−1580 cm^{-1} (G band). The intensity ratio (I_D/I_G) was found to correlate linearly with the sp^2/sp^3 ratio.[32] According to our Raman examination, these two bands became more prominent when more starch was used as a carbon source when forming the CFO@a-C. Their ratio increased initially until reaching a maximum value of 7.65 with approximately 0.1 g of starch precursor before obviously decreasing when additional starch content was used. Such a change suggests that carbons far from their CFO/carbon heterointerfaces are predominantly sp^3-bonded. In our study, we infer that the existence of sp^2 in carbon shells may play a key role in acting as the electron or hole transport layer.

3.3. TGA and M−H Loops Measurement. Carbonaceous matter was formed through hydrothermal carbonization, and the amount of such matter involved in CFO encapsulation was estimated based on the thermogravimetric weight loss in a thermogravimetric analysis. In particular, the TGA analysis, shown in Figure 4a, revealed abrupt weight loss between 500 and 600 °C for the encapsulated samples, which was ascribed to the thermal decomposition of carbon.[10,33] The mass loss of these CFO@a-C samples increased with increasing amount of starch during the hydrothermal process. The magnetization (M) versus field (H) curves at room temperature in Figure 4b show that the induced magnetization at the highest field value ($M_{max.}$) increased initially and reached a maximum value of 82.8 emu/g, which is slightly higher than those of other CFO nanoparticle samples (up to 79 emu/g) and reveals the magnetic enhancement of CFO after carbon encapsulation. The measured $M_{max.}$ and the one corrected based on the thermogravimetric loss are depicted in Figure 4c, showing up to 25% magnetic enhancement.

3.4. Soft X-ray L-Edge Absorptions. The element- and site-specific electronic variations underlying these exceptional observations were thoroughly examined based on synchrotron X-ray absorption spectroscopy (XAS) and X-ray magnetic circular dichroism (XMCD). Spectra were measured under the variations in incident helicities switching, caused by an undulator, parallel (μ^+) or antiparallel (μ^-) to the sample magnetization with an applied magnetic field of 1.5 T parallel to the incident X-rays. The XAS spectra (μ_0) were obtained as an average, $\mu_0 = (\mu^+ + \mu^-)/2$, as per standard procedure.[34,35]

In Figure 5a, nonsignificant variations were observed between the Fe L-edge XAS results of CFO and CFO@a-C. The carbon coating primarily affected the Co L-XAS results, which revealed a systematic trend, as depicted in Figure 5b. Specifically, this figure presents the results of the ligand field multiplet (LFM) calculations of the high-spin $2p^63d_{HS}^{7}(^4T_1) \rightarrow 2p^53d^8(^3A_2)$ transition (thin black lines) along with the experimental data corresponding to CoO (solid circle). The overall line shape of our results resembles that of high-spin Co^{2+} ions in an oxygen octahedron. Referring to de Groot's results, the LFM calculations in ref 36 suggest that the spin−orbital coupling (83 meV) and cubic ligand field strength (0.9 eV) lifted four states, at energies of 0 (E_2), 44 (G), 115 (G^*), and 128 meV (E_1). With an increase in the amount of carbon, the L-edge absorptions revealed signatures, particularly for Co L_2, of a transition from E_2 to G symmetry. Note that L-edge XAS is affected by the structure of the target complex, local metal−ligand coordination, and intra-atomic Coulombic and spin−orbit interactions in the 2p core and 3d valence orbitals.[37−39] The transition (from E_2 to G symmetry) shown in Figure 5b indicates the variations in the spin−orbit interactions of the absorption process, $2p^63d_{HS}^{7-\delta}(^4T_1) \rightarrow 2p^53d^{8-\delta}(^3A_2)$, when the valence holes (δ) are introduced by carbon−sp contact. The presence of these holes explains the higher-energy shift of peak (peak A, Figure 5b, inset)

https://doi.org/10.1021/acs.jpcc.3c03046
J. Phys. Chem. C 2023, 127, 17978−17986

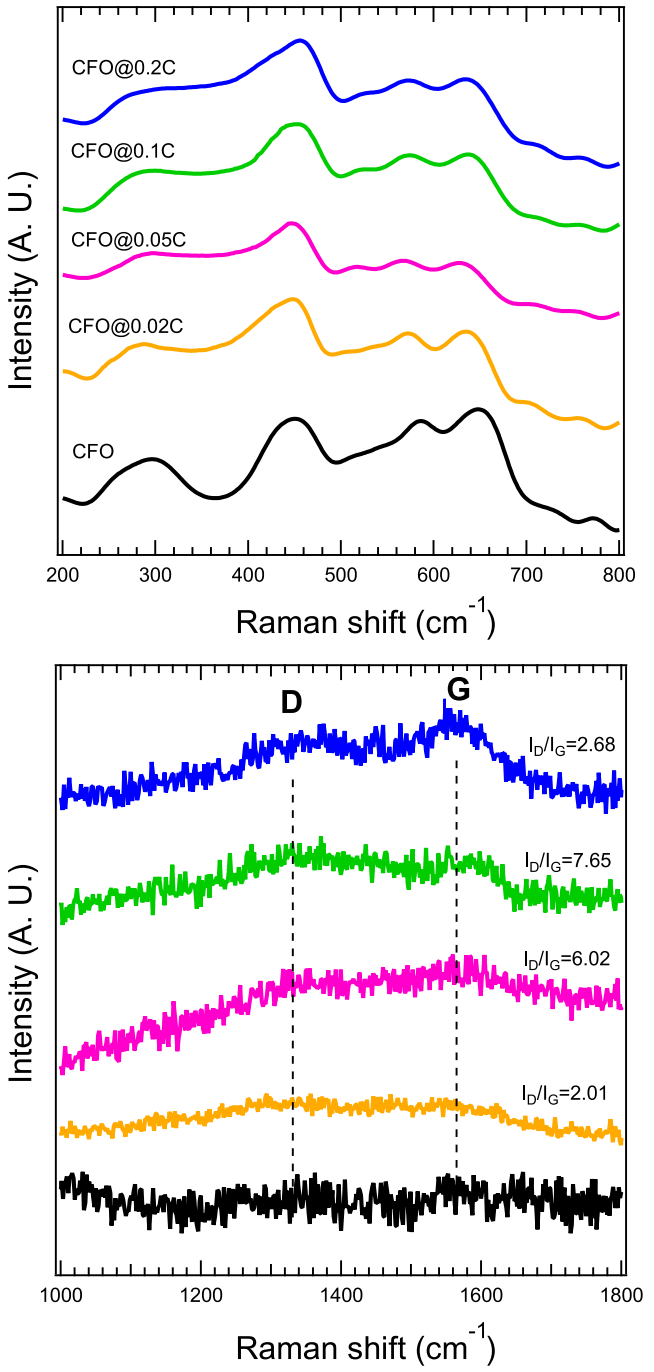

Figure 3. Comparison of low-wavenumber (top) and high-wavenumber (bottom) regions of the Raman spectra of all of the test samples. The intensity ratio (I_D/I_G) is also shown.

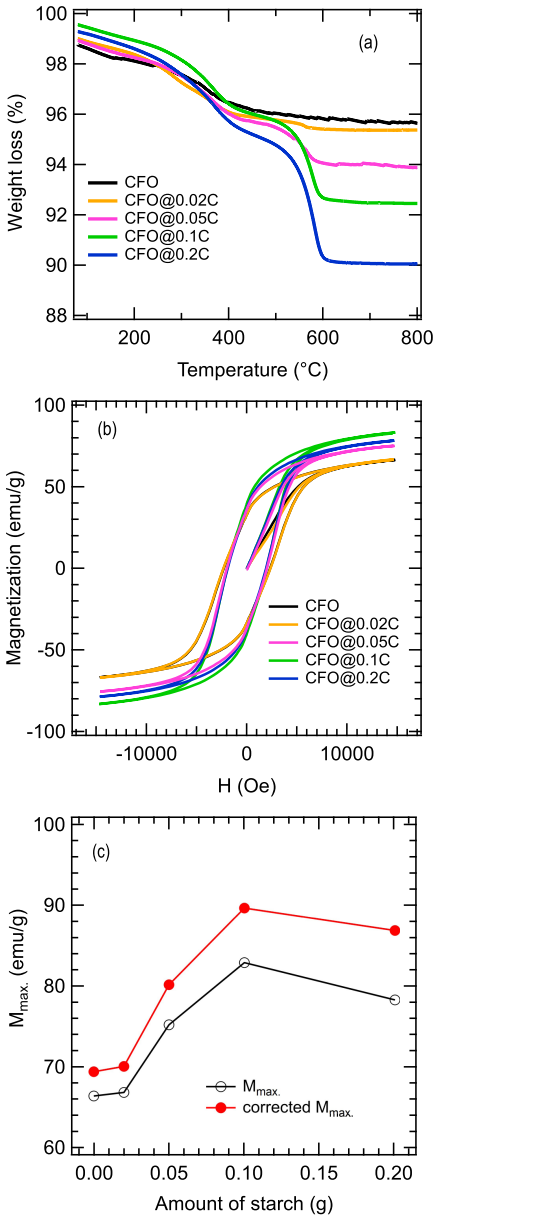

Figure 4. (a) TGA curves of test CFO@a-C samples. (b) $M-H$ curves. (c) The induced magnetization at the highest field ($M_{max.}$) of various cobalt ferrite samples. The magnetization was corrected based on the thermogravimetric loss.

immediately above the absorption edge, which indicates an increase in the metal oxidation state.[40−43] These observations implied hole injection upon carbon coating and characterized the type of hole acceptor for the Co^{2+} ions.

3.5. Soft X-ray L-Edge XMCD. Figure 6a,b shows the Fe and Co $L_{2,3}$-edge XAS spectra with photon helicity of incident X-ray parallel (μ^+) and antiparallel (μ^-) to the direction of sample magnetization, respectively. The XAS results lead to the same conclusion as the Co L-edge XAS results: the carbon coating alters the spin−orbit coupling corresponding to L-edge XAS results: the carbon coating alters the spin−orbit coupling corresponding to $2p^63d_{HS}^7$ ($^4T_1$). The polarization- and the site-specific distribution of holes injected because of carbon−sp contact can be further examined by using the Co and Fe L-edge absorption spectra. The spectral features in polarization dependence, $L_{2,3}$-XMCD and L_3-XMCD, as shown in Figure 6, are consistent with previous works reported elsewhere.[44−46]

In Figure 6a, features a_2 and b_2 of opposite XMCD signs in the Co L_3-edge XMCD spectra are associated with the Co^{2+} ions at the tetrahedral (Co^{2+}_{tet}) and octahedral (Co^{2+}_{oct}) sites,[47] respectively, and correspond to the Néel arrangement of the Co^{2+}_{tet} and Co^{2+}_{oct}. The overall MCD signals of the samples were categorized into two groups: one including CFO, CFO@0.02C, and CFO@0.05C, and the other including CFO@0.1C and CFO@0.2C that were referred to as E_2 and G symmetry, respectively, according to Figure 5b. Thus, the enhancement b_2 in the XMCD signal has indicated an $E_2 \rightarrow G$ transition with

https://doi.org/10.1021/acs.jpcc.3c03046
J. Phys. Chem. C 2023, 127, 17978−17986

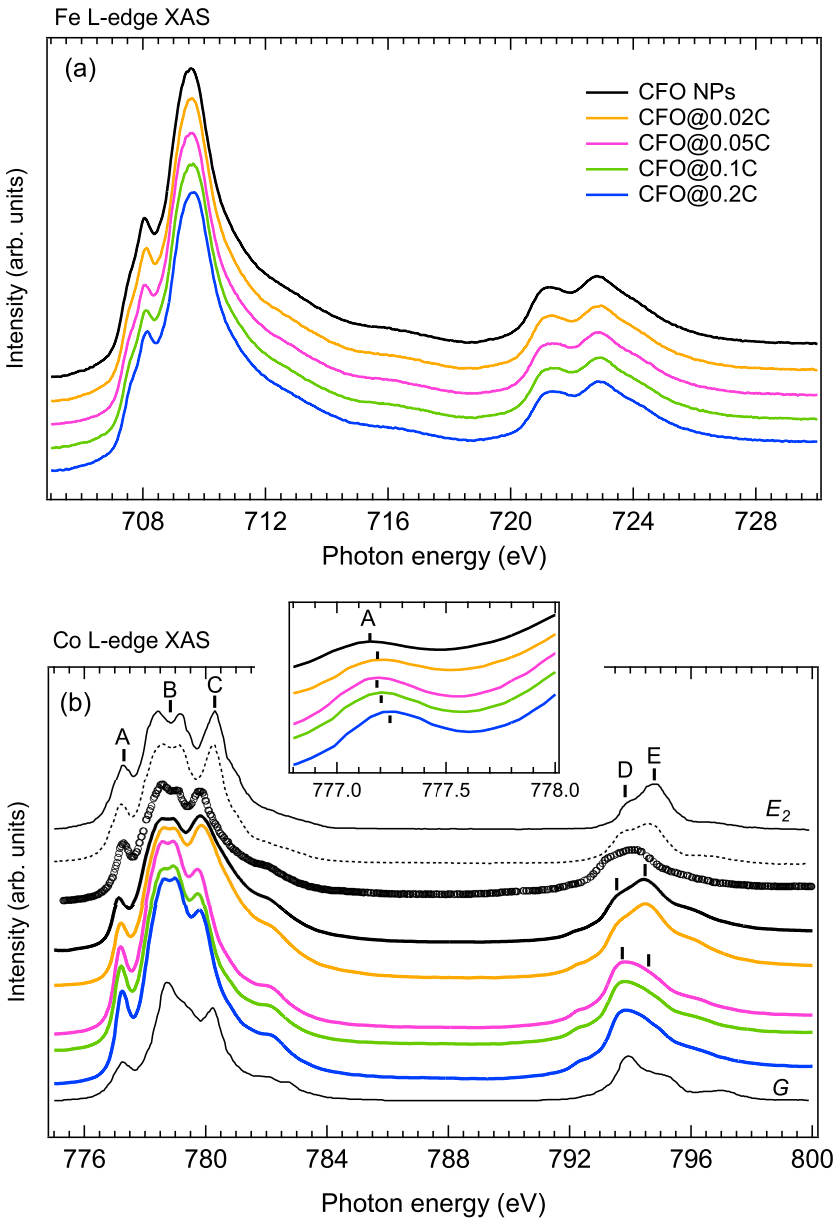

Figure 5. (a) Fe L-edge soft X-ray absorption (L-XAS) exhibited by cobalt ferrite nanoparticles (CFO NPs) as a function of the amount of starch. (b) Co L-XAS as a function of the amount of starch. The inset shows an enlarged view of feature *A*. E_2 and *G* (thin black): theoretical L-XAS spectra (reproduced with permission from ref [36]. copyright 1994 Elsevier) for the Co^{2+} high-spin $3d^7 \rightarrow 2p^5 3d^8$ transition with (solid thin black) and without (dashed) the consideration of spin−orbit coupling. Black circle: experimental spectrum of CoO (Reproduced with permission from ref [36]. copyright 1994 Elsevier).

the increase of polarized holes at the Co_{oct}^{2+} that engendered the magnetic enhancement.

XMCD can distinguish Fe ions with different valences (Fe^{3+} and Fe^{2+}) at different lattice sites in spinel structure.[48] In Figure 6b, the L_3-edge XMCD signal of the positive component (labeled as a_3) is corresponding to the Fe^{3+} ions in the tetrahedral sites. And two strong negative components (labeled as b_2 and b_3) are related to the Fe^{2+} and Fe^{3+} ions in the octahedral sites, respectively. The opposite direction between peak a_3 and peak b_2, b_3 shows the antiferromagnetic interaction of Fe ions at tetrahedral and octahedral sites, namely, $[Fe^{3+}]_{tet\downarrow}[Fe^{2+}Fe^{3+}]_{oct\uparrow}O_4$ based on a simplified ionic scheme. The holes also increased in line with the MCD features (a_3 and b_3) representing Fe_{tet}^{3+} and Fe_{oct}^{3+} with opposite spin directions, although no significant variations in Fe L-edge XAS were concluded.

3.6. First-Principles Calculations. The microscopic origin of the magnetic enhancement in CFO@a-C was further investigated based on a first-principles approach. The Vienna Ab initio Simulation Package[49] implementation of density functional theory (DFT) was used to calculate the effect of hole acceptors by computing electronic variations under neutral and charged states of the equilibrium lattice. To ensure the purely electronic effect on the magnetic enhancement, we evaluated a partial spinel in addition to an ideal inverse spinel cobalt ferrite. The experimental approach has reported that ≈20% of Co^{2+} in the tetrahedral sublattice stabilized the partial spinel.[20,50] Based on the generalized gradient approach with Hubbard correction (GGA + *U*)

https://doi.org/10.1021/acs.jpcc.3c03046
J. Phys. Chem. C 2023, 127, 17978−17986

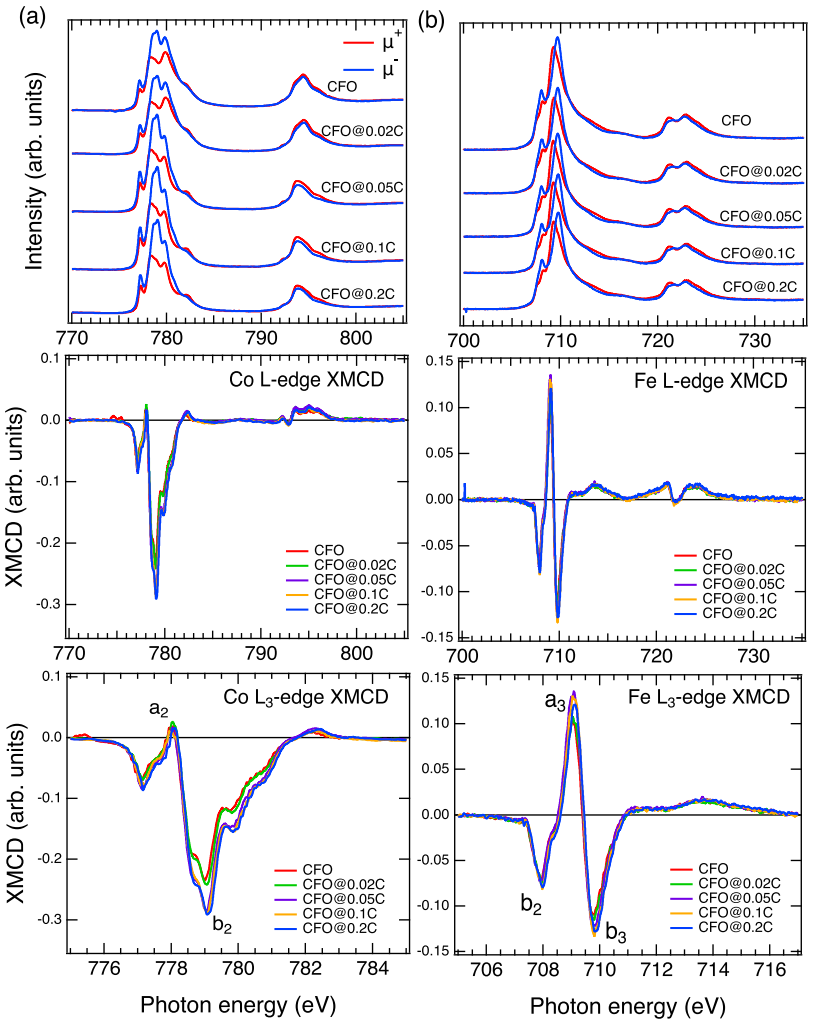

Figure 6. L-edge X-ray absorption (L-XAS) and L-edge X-ray magnetic circular dichroism L-XMCD spectrum corresponding to (a) Co and (b) Fe under right and left circular polarization parallel (μ^+) and antiparallel (μ^-) to the sample magnetization. The top, middle, and lower panels, respectively, show the polarization-dependent L-XAS, L-XMCD, and L_3-XMCD.

method,[51] the partial spinel $(Co_{1-x}Fe_x)_{tet\downarrow}(Co_xFe_{2-x})_{oct\uparrow}O_4$ x = 0.75 has been theoretically shown to be energetically favorable than fully inverse spinel (x = 1.0). In the ideal inverse spinel, the Fe and Co octahedra comprised the B1 and B2 sublattices in the octahedral site and had shearing corners along $\langle 1\bar{1}0\rangle$ and $\langle 110\rangle$ in a conventional lattice ($Fd\bar{3}m$, 56 atoms). The partial spinel (x = 0.75) comprised a doubled primitive lattice (28 atoms), wherein a Fe tetrahedron was exchanged with a Co octahedron. Dudarev's simplified GGA + U scheme[52,53] was adopted in this work. The initial magnetic moment corresponding to the Néel-type arrangement of the octahedral and tetrahedral sublattices was chosen for both the structure optimization and electronic calculation. Equilibrium lattice was obtained from internal coordinates relaxation with a 3 × 3 × 3 (x = 0.75) and a 4 × 4 × 4 (x = 1) Monkhorst−Pack k-mesh, respectively, until the forces on each ion are converged to less than 2 meV/Å. Energy cutoff of 520 eV was set. U_{eff} was set to 3.4 and 3.1 eV for the Fe and Co ions, respectively; the electronic bandgap consists of previous calculations[54,55] for stoichiometric $CoFe_2O_4$ and is in reasonable agreement with prior conductivity measurements.[56] Figure 7 shows the variations in the electronic structure as a function of charged states. The corresponding variations on the computed d electrons and the magnetization are shown in Figure 8. The solutions of the equilibrium configurations of both spinels are magnetic insulators.[51] The charged states, + and ++, of both x = 0.75 and x = 1.0 spinels reveal consistent results with those for the spin-minority state of Co ions in octahedral (Co_{oct}) upon which the hole doping occurs. In partial spinel (x = 0.75), the computed magnetization of Co_{oct} boosts up before that of Co_{td}. The d hole introduced by the charged states + and ++ are increased by 9.8 and 19.6% for Co_{oct}, and 3.8 and 8.6% for Co_{tet}. The variations on magnetization and charge in Fe ions are an order of magnitude smaller than that of Co ions. The calculation results have suggested the hole doping upon the Co_{oct} spin minority dominates the enhancement of magnetization and also reveal that the total magnetic moment is increased for the charged states of both x = 0.75 and x = 1.0, demonstrating the purely electronic effect accounting for the magnetization enhancement apart from other extrinsic causes.

4. DISCUSSIONS

We are aware that one of the mechanisms for magnetic enhancement in spinel ferrites is cationic redistribution: the cations migrated from one site to another by replacing the other cations. The size or surface effects may result in cationic redistribution and affect the magnetic properties of CFO

https://doi.org/10.1021/acs.jpcc.3c03046
J. Phys. Chem. C 2023, 127, 17978−17986

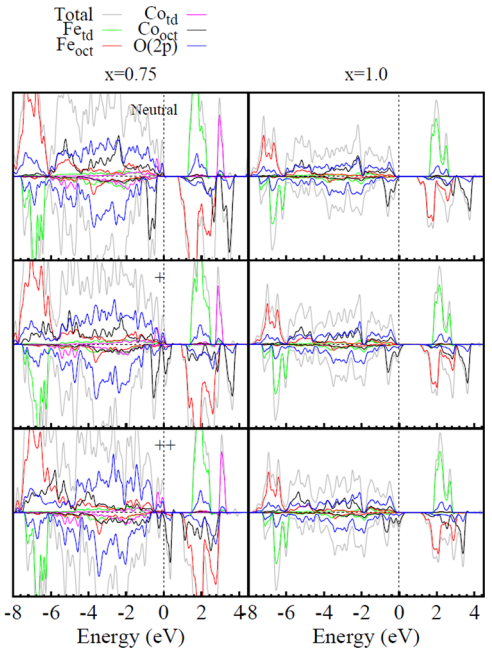

Figure 7. Calculated electronic structure variations as a function of neutral (0) and charged states (+ and ++) for $(Co_{1-x}\ Fe_x)_{tet\downarrow}\ [Co_x\ Fe_{2-x}]_{oct\uparrow}\ O_4$ (x = 0.75 and x = 1). The majority (minority) spin density of states is set as positive (negative).

nanoparticles.[57,58] In the present work, if the cation redistribution to be responsible for the observed magnetic enhancement, the feature intensities of XMCD at octahedral and tetrahedral sites would be changed, e.g., the intensity of one site would increase and that of the other site may decrease. In Figure 6a, the intensity of b_2 (Co^{2+}_{oct}) in the Co XMCD spectra increased but that of a_2 (Co^{2+}_{tet}) nearly remained the same. The XMCD results evidently ruled out the observed magnetic enhancement, possibly due to Co cationic redistribution because the features designated to $Co^{2+}_{tet.}$ are unaffected by the carbon encapsulation using low-temperature annealing. In addition, as displayed in Figure 6b, the a_3 (Fe^{2+}_{oct}) intensity increased to the same extent as b_3 (Fe^{2+}_{oct}) in the Fe L_3-XMCD spectra, suggesting magnetic enhancement due to hole injection upon Fe ions are canceled because of the opposite sign of XMCD signal. Therefore, no signatures of cation redistribution are indicated by the L-XMCD spectrum. Magnetic enhancement in CFO@a-C due to hole injection upon octahedral Co is concluded.

5. CONCLUSIONS

Based on the soft X-ray absorption results and GGA + U calculations, we concluded that the hole reservoir, namely, the octahedral Co of spin-minority states in a cobalt ferrite, controls the magnetic enhancement in the CFO@a-C NPs hybrid system. In a prior study by the present authors,[19] magnetic enhancement in Fe_3O_4@a-C NPs was unraveled using synchrotron spectroscopy. The electronic states of Fe^{3+} (d^5) in a tetrahedral sublattice of Fe_3O_4 are represented by $e^{2\downarrow}t_2^{3\downarrow}$. A simplified ionic scheme, namely, $e^{2\downarrow}\ t_2^{3\downarrow} \rightarrow e^{2\downarrow}\ t_2^{3\downarrow}\ e^{\uparrow}$, elucidated both results obtained from the Fe K-edge X-ray absorption near-edge structure and the Fe L_3-XMCD. The tetrahedral Fe ions, which served as electron acceptors, engender the magnetic enhancement in a Fe_3O_4@a-C hybrid system. In contrast to the previous Fe_3O_4@a-C case, in the present study, magnetic enhancement was attributed to octahedral Co ions, which served as hole acceptors in a CFO@a-C hybrid system. These observations confirmed that magnetic enhancement can be achieved in a spinel ferrite

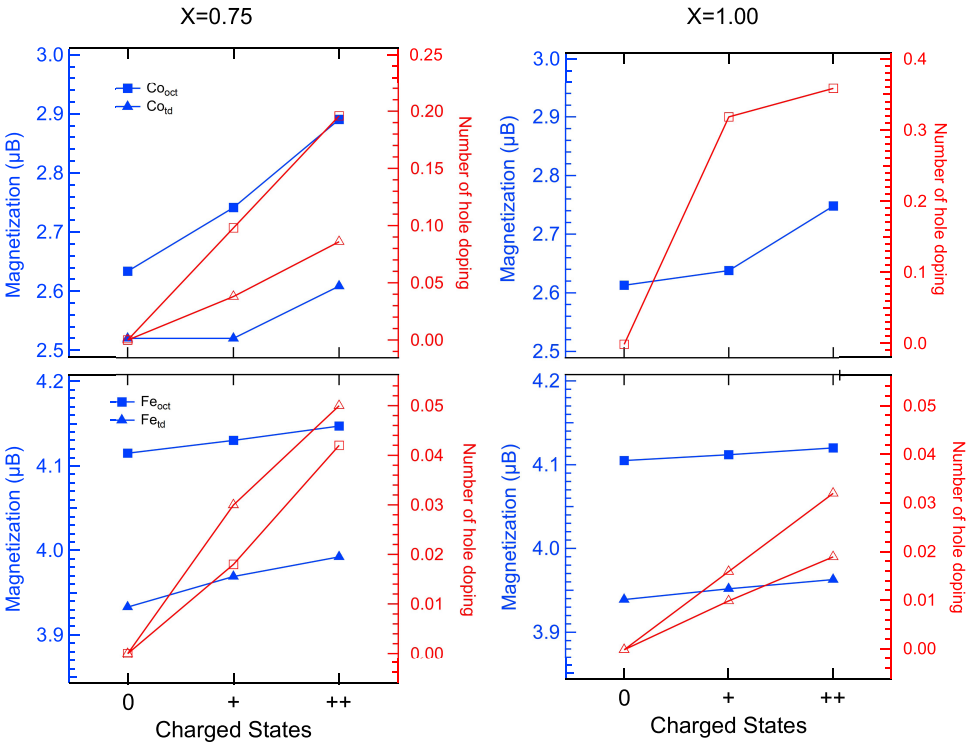

Figure 8. DFT + U computed magnetization and 3d hole doping (in average) for each crystallographic site for the neutral (0) and charged states (+ and ++) of the $(Co_{1-x}\ Fe_x)_{tet\downarrow}\ [Co_x\ Fe_{2-x}]_{oct\uparrow}\ O_4$ (x = 0.75 and x = 1). Numerical values are listed in the Supporting information.

https://doi.org/10.1021/acs.jpcc.3c03046
J. Phys. Chem. C 2023, 127, 17978−17986

system by using a cost-effective a-C encapsulation process. Moreover, our results indicated the spin-polarized states in a spinel ferrite under carbon−sp contact can serve as electron donors or acceptors in response to magnetic enhancement.

■ ASSOCIATED CONTENT

Data Availability Statement

The data supporting the findings of this study are available within the article.

Supporting Information

The Supporting Information is available free of charge at https://pubs.acs.org/doi/10.1021/acs.jpcc.3c03046.

Final Rietveld plots of XRD profiles of CFO and CFO@0.2C samples using GSAS software and EXPGUI interface; numerical table of DFT + U computed averaged 3d charges and magnetization in each crystallographic site for the neutral (0) and charged states (+ and ++) of the $(Co_{1-x}Fe_x)_{tet\downarrow}[Co_xFe_{2-x}]_{oct\uparrow}O_4$ (x = 0.75 and x = 1) (PDF)

■ AUTHOR INFORMATION

Corresponding Authors

Wen-Bin Wu − *National Synchrotron Radiation Research Center, Hsinchu 30076, Taiwan*; Email: frankwu@nsrrc.org.tw

Jiunn Chen − *Department of Applied Physics, National Pingtung University, Pingtung 90003, Taiwan*; orcid.org/0000-0001-5601-5293; Email: asesrrc@gmail.com

Authors

Jiann-Shing Lee − *Department of Applied Physics, National Pingtung University, Pingtung 90003, Taiwan*

Shih-Min Hung − *Department of Applied Physics, National Pingtung University, Pingtung 90003, Taiwan*

Chun-Rong Lin − *Department of Applied Physics, National Pingtung University, Pingtung 90003, Taiwan*; orcid.org/0000-0003-4880-6196

Chi-Liang Chen − *National Synchrotron Radiation Research Center, Hsinchu 30076, Taiwan*; orcid.org/0000-0001-8509-0655

Jau-Wern Chiou − *Department of Applied Physics, National University of Kaohsiung, Kaohsiung 81148, Taiwan*

Chih-Yu Hua − *National Synchrotron Radiation Research Center, Hsinchu 30076, Taiwan*

Huang-Ming Tsai − *National Synchrotron Radiation Research Center, Hsinchu 30076, Taiwan*

Way-Faung Pong − *Department of Physics, Tamkang University, New Taipei City 251301, Taiwan*

Chien-Te Chen − *National Synchrotron Radiation Research Center, Hsinchu 30076, Taiwan*

Complete contact information is available at: https://pubs.acs.org/10.1021/acs.jpcc.3c03046

Notes

The authors declare no competing financial interest.

■ ACKNOWLEDGMENTS

The authors thank the Ministry of Science and Technology, ROC, for financially supporting this research (MOST 110-2112-M-153-006). The authors also gratefully acknowledge the use of HRTEM (EM000800) of MOST 110-2731-M-006-001.

■ REFERENCES

(1) Bartůněk, V.; Sedmidubsky, D.; Huber, S.; Svecova, M.; Ulbrich, P.; Jankovsky, O. Synthesis and Properties of Nanosized Stoichiometric Cobalt Ferrite Spinel. *Materials* **2018**, *11*, 1241.

(2) Yasmin, N.; Abdulsatar, S.; Hashim, M.; Zahid, M.; Gillani, S. F.; Kalsoom, A.; Ashiq, M. N.; Inam, I.; Safdar, M.; Mirza, M. Structural and magnetic studies of Ce-Mn doped M-type $SrFe_{12}O_{19}$ hexagonal ferrites by sol-gel auto-combustion method. *J. Magn. Magn. Mater.* **2019**, *473*, 464−469.

(3) Nikitin, M. P.; Orlov, A. V.; Znoyko, S. L.; Bragina, V. A.; Gorshkov, B. G.; Ksenevich, T. I.; Cherkasov, V. R.; Nikitin, P. I. Multiplex biosensing with highly sensitive magnetic nanoparticle quantification method. *J. Magn. Magn. Mater.* **2018**, *459*, 260−264.

(4) Yu, Y. S.; Deng, G. C.; Cao, Y. M.; McIntyre, G. J.; Li, R. B.; Yuan, N.; Feng, Z. J.; Ge, J. Y.; Zhang, J. C.; Cao, S. X. Tuning the magnetic anisotropy via Mn substitution in single crystal $Co_4Nb_2O_9$. *Ceram. Int.* **2019**, *45*, 1093−1097.

(5) Jiang, S.; Qian, K.; Yu, K. J.; Zhou, H. F.; Weng, Y. X.; Zhang, Z. W. Controllable synthesis and microwave absorption properties of Fe_3O_4@f-GNPs nanocomposites. *Compos. Commun.* **2020**, *20*, No. 100363.

(6) Zhou, J.; Shu, X. F.; Wang, Y. Q.; Ma, J. L.; Liu, Y.; Shu, R. W.; Kong, L. B. Enhanced microwave absorption properties of (1-x)$CoFe_2O_4$/xCoFe composites at multiple frequency bands. *J. Magn. Magn. Mater.* **2020**, *493*, No. 165699.

(7) Liu, X.; Xiong, L.; Yu, X.; He, S.; Zhang, B.; Shen, J. Magnetically controlled terahertz modulator based on Fe_3O_4 nanoparticle ferrofluids. *J. Phys. D: Appl. Phys.* **2018**, *51*, No. 105003.

(8) Shokrollahi, H. A review of the magnetic properties, synthesis methods and applications of maghemite. *J. Magn. Magn. Mater.* **2017**, *426*, 74−81.

(9) Valenzuela, R. Novel Applications of Ferrites. *Phys. Res. Int.* **2012**, *2012*, No. 591839.

(10) Yin, P.; Zhou, W.; Zhang, X.; Guo, B.; Li, P. Bio-Based Thermoplastic Starch Composites Reinforced by Dialdehyde Lignocellulose. *Molecules* **2020**, *25*, 3236.

(11) Sugimoto, M. The past, present, and future of ferrites. *J. Am. Ceram. Soc.* **1999**, *82*, 269−280.

(12) Hazra, S.; Ghosh, N. N. Preparation of nanoferrites and their applications. *J. Nanosci. Nanotechnol.* **2014**, *14*, 1983−2000.

(13) Dippong, T.; Levei, E. A.; Cadar, O. Recent Advances in Synthesis and Applications of MFe_2O_4 (M = Co, Cu, Mn, Ni, Zn) Nanoparticles. *Nanomaterials* **2021**, *11*, 1560.

(14) Basavaiah, K.; Rao, A. V. P. One-pot synthesis of superparamagnetic polyaniline microtubes and magnetite nanoparticles via self-assembly method. *Curr. Nanosci.* **2012**, *8*, 215−220.

(15) Fidale, L. C.; Nikolajski, M.; Rudolph, T.; Dutz, S.; Schacher, F. H.; Heinze, T. Hybrid Fe_3O_4@amino cellulose nanoparticles in organic media heterogeneous ligands for atom transfer radical polymerizations. *J. Colloid Interface Sci.* **2013**, *390*, 25−33.

(16) Jingting, C.; Huining, L.; Yi, Z. Preparation and characterization of magnetic nanoparticles containing Fe_3O_4-dextran- anti-β-human chorionic gonadotropin, a new generation choriocarcinoma-specific gene vector. *Int. J. Nanomed.* **2011**, *6*, 285−294.

(17) Seo, W. S.; Lee, J. H.; Sun, X.; Suzuki, Y.; Mann, D.; Liu, Z.; Terashima, M.; Yang, P. C.; McConnell, M. V.; Nishimura, D. G.; Dai, H. FeCo/graphitic-shell nanocrystals as advanced magnetic-resonance-imaging and near-infrared agents. *Nat. Mater.* **2006**, *5*, 971−976.

(18) Lee, J.-S.; Song, Y.-J.; Hsu, H.-S.; Lin, C.-R.; Huang, J.-Y.; Chen, J. Magnetic enhancement of carbon-encapsulated magnetite nanoparticles. *J. Alloys Compd.* **2019**, *790*, 716−722.

(19) Lee, J.-S.; Wu, W.-B.; Chen, J.; Chen, C.-L.; Kuo, H.-W.; Lin, C.-R.; Lin, H.-J.; Chen, C.-T. Carbon encapsulation of magnetite nanoparticles enhances magnetism at roomtemperature due to spin-polarized charge transfer. *Appl. Phys. Lett.* **2021**, *118*, No. 072403.

(20) Sawatzky, G. A.; Van Der Woude, F.; Morrish, A. H. Mossbauer Study of Several Ferrimagnetic Syinels. *Phys. Rev.* **1969**, *187*, 747.

(21) Maaz, K.; Mumtaz, A.; Hasanain, S. K.; Ceylan, A. Synthesis and magnetic properties of cobalt ferrite ($CoFe_2O_4$) nanoparticles prepared by wet chemical route. *J. Magn. Magn. Mater.* **2007**, *308*, 289−295.
(22) Rao, K. S.; Choudary, G. S.; Rao, K. H.; Sujatha, C. Structural and Magnetic Properties of Ultrafine $CoFe_2O_4$ Nanoparticles. *Procedia Mater. Sci.* **2015**, *10*, 19−27.
(23) Sayyar, S.; Aslibeiki, B.; Asgari, A. CoFe2O4 bulk, nanoparticles and layer: A comparison of structural, magnetic, and optical properties. *Prog. Phys. Appl. Mater.* **2022**, *2*, 165−173.
(24) Wang, W. H.; Ren, X. Flux growth of high-quality CoFe2O4 single crystals and their characterization. *J. Cryst. Growth* **2006**, *289*, 605−608.
(25) Chakraborty, S.; Sahoo, B.; Teraoka, I.; Miller, L. M.; Gross, R. A. Enzyme-Catalyzed Regioselective Modification of Starch Nanoparticles. *Macromolecules* **2005**, *38*, 61−68.
(26) Rafiee, E.; Khodayari, M. Starch as a green source for Fe3O4@carbon core−shell nanoparticles synthesis: a support for 12-tungstophosphoric acid, synthesis, characterization, and application as an efficient catalyst. *Res. Chem. Intermed.* **2016**, *42*, 3523−3536.
(27) Dong, C.-L.; Chiou, J.-W.; Tsai, H.-M.; Fu, H.-W.; Lin, H.-J.; Chen, C. T.; Pong, W.-F. Photon-In/Photon-Out Soft X-ray Spectroscopy at the TPS 45A Beamline. *Synchrotron Radiat. News* **2017**, *30*, 24−29.
(28) Tsai, H.-M.; Fu, H.-W.; Kuo, C.-Y.; Huang, L.-J.; Lee, C.-S.; Hua, C.-Y.; Kao, K.-Y.; Lin, H.-J.; Fung, H.-S.; Chung, S.-C.; et al. A submicron soft X-ray active grating monochromator beamline for ultra-high resolution angle-resolved photoemission spectroscopy. *AIP Conf. Proc.* **2019**, *2054*, No. 060047.
(29) Chandramohan, P.; Srinivasan, M. P.; Velmurugan, S.; Narasimhan, S. V. Cation distribution and particle size effect on Raman spectrum of CoFe2O4. *J. Solid State Chem.* **2011**, *184*, 89−96.
(30) Testa-Anta, M.; Rivas-Murias, B.; Salgueiriño, V. Spin frustration drives exchange bias sign crossover in $CoFe_2O_4$−Cr_2O_3 nanocomposites. *Adv. Funct. Mater.* **2019**, *29*, No. 1900030.
(31) Rivas-Murias, B.; Testa-Anta, M.; Skorikov, A. S.; Comesaña-Hermo, M.; Bals, S.; Salgueiriño, V. Interfaceless exchange bias in CoFe2O4 nanocrystals. *Nano Lett.* **2023**, *23*, 1688−1695.
(32) Lee, S.-C.; Tai, F.-C.; Wei, C.-H. Correlation between sp2/sp3 Ratio or Hydrogen Content and Water Contact Angle in Hydrogenated DLC Film. *Mater. Trans.* **2007**, *48*, 2534−2538.
(33) Shahverdi, A.; Kim, K. S.; Alinejad, Y.; Soucy, G.; Mostaghimi, J. Selective oxidation of excess amorphous carbon during single-walled carbon nanotubes synthesis by induction thermal plasma proces. *J. Nano Res.* **2009**, *2*, 800−812.
(34) Chen, C. T.; Idzerda, Y. U.; Lin, H.-J.; Smith, N. V.; Meigs, G.; Chaban, E.; Ho, G. H.; Pellegrin, E.; Sette, F. Experimental Confirmation ofthe X-Ray Magnetic Circular Dichroism Sum Rules for Iron and Cobalt. *Phys. Rev. Lett.* **1995**, *75*, No. 152.
(35) Thole, B. T.; Carra, P.; Sette, F.; van der Laan, G. X-Ray Circular Dichroism as a Probe of Orbital Magnetization. *Phys. Rev. Lett.* **1992**, *68*, 1943.
(36) de Groot, F. X-ray absorption and dichroism of transition metals and their compounds. *J. Electron Spectrosc. Relat. Phenom.* **1994**, *67*, 529−622.
(37) Laan, G. v. d.; Kirkman, I. W. The 2p absorption spectra of 3d transition metal compounds in tetrahedral and octahedral symmetry. *J. Phys.: Condens. Matter* **1992**, *4*, 4189.
(38) Martins, M.; Godehusen, K.; Richter, T.; Wernet, P.; Zimmermann, P. Open shells and multi-electron interactions: core level photoionization of the 3d metal atoms. *J. Phys. B: At., Mol. Opt. Phys.* **2006**, *39*, R79.
(39) Thole, B. T.; Laan, G. v. d. Branching ratio in X-ray absorption spectroscopy. *Phys. Rev. B* **1988**, *38*, 3158.
(40) Kubin, M.; Kern, J.; Gul, S.; Kroll, T.; Chatterjee, R.; Löchel, H.; Fuller, F. D.; Sierra, R. G.; Quevedo, W.; Weniger, C.; et al. Soft X-ray absorption spectroscopy of metalloproteins and high-valent metal-complexes at room temperature using free-electron lasers. *Struct. Dyn.* **2017**, *4*, No. 054307.
(41) Cramer, S. P.; DeGroot, F. M. F.; Ma, Y.; Chen, C. T.; Setter, F.; Kipke, C. A.; Eichhorn, D. M.; Chan, M. K.; Armstrong, W. H.; Libby, E.; et al. Ligand Field Strengths and Oxidation States from Manganese L-Edge Spectroscopy. *J. Am. Chem. Soc.* **1991**, *113*, 7937−7940.
(42) Gorlin, Y.; Chung, C.-J.; Nordlund, D.; Clemens, B. M.; Jaramillo, T. F. Mn_3O_4 Supported on Glassy Carbon: An Active Non-Precious Metal Catalyst for the Oxygen Reduction Reaction. *ACS Catal.* **2012**, *2*, 2687−2694.
(43) Ebrahimizadeh Abrishami, M.; Risch, M.; Scholz, J.; Roddatis, V.; Osterthun, N.; Jooss, C. Oxygen Evolution at Manganite Perovskite Ruddlesden-Popper Type Particles: Trends of Activity on Structure, Valence and Covalence. *Materials* **2016**, *9*, 921.
(44) Wang, B. Y.; Wang, H. T.; Singh, S. B.; Shao, Y. C.; Wang, Y. F.; Chuang, C. H.; Yeh, P. H.; Chiou, J. W.; Pao, C. W.; Tsai, H. M.; et al. Effect of geometry on the magnetic properties of $CoFe_2O_4$−$PbTiO_3$ multiferroic composites. *RSC Adv.* **2013**, *3*, 7884−7893.
(45) Moyer, J. A.; Vaz, C. A. F.; Arena, D. A.; Kumah, D.; Negusse, E.; Henrich, V. E. Magnetic structure of Fe-doped CoFe2O4 probed by X-ray magnetic spectroscopies. *Phys. Rev. B* **2011**, *84*, No. 054447.
(46) Kim, C. H.; Myung, Y.; Cho, Y. J.; Kim, H. S.; Park, S. H.; Park, J.; Kim, J.-Y.; Kim, B. Electronic Structure of Vertically Aligned Mn-Doped $CoFe_2O_4$ Nanowires and Their Application as Humidity Sensors and Photodetectors. *J. Phys. Chem. C* **2009**, *113*, 7085.
(47) Sette, F.; Chen, C. T.; Ma, Y.; Modesti, S.; Smith, N. V. Magnetic Circular Dichroism Studies with Soft X-rays. *AIP Conf. Proc.* **1990**, 787−795.
(48) Chang, C. F.; Hu, Z.; Klein, S.; Liu, X. H.; Sutarto, R.; Tanaka, A.; Cezar, J. C.; Brookes, N. B.; Lin, H.-J.; Hsieh, H. H.; et al. Dynamic Atomic Reconstruction: How Fe_3O_4 Thin Films Evade Polar Catastrophe for Epitaxy. *Phys. Rev. X* **2016**, *6*, No. 041011.
(49) Kresse, G.; Hafner, J. Ab. initio molecular dynamics for liquid metals. *Phys. Rev. B* **1993**, *47*, 558.
(50) Braicovich, L.; Tagliaferri, A.; Laan, G. v. d.; Ghiringhelli, G.; Brookes, N. B. Sum Rules in X-Ray Resonant Raman Scattering: Recovering the Co Ground State Information in $CoFe_2O_4$ as a Test Case. *Phys. Rev. Lett.* **2003**, *90*, No. 117401.
(51) Hou, Y. H.; Zhao, Y. J.; Liu, Z. W.; Yu, H. Y.; Zhong, X. C.; Qiu, W. Q.; Zeng, D. C.; Wen, L. S. Structural, electronic and magnetic properties of partially inverse spinel CoFe2O4: a first principles study. *J. Phys. D: Appl. Phys.* **2010**, *43*, No. 445003.
(52) Perdew, J. P.; Burke, K.; Ernzerhof, M. Generalized Gradient Approximation Made Simple. *Phys. Rev. Lett.* **1996**, *77*, 3865.
(53) Dudarev, S. L.; Botton, G. A.; Savrasov, S. Y.; Humphreys, C. J.; Sutton, A. P. Electron-energy-loss spectra and the structural stability of nickel oxide: An LSDA+U study. *Phys. Rev. B* **1998**, *57*, 1505.
(54) Antonov, V. N.; Harmon, B. N.; Yaresko, A. N. Electronic structure and X-ray magnetic circular dichroism in Fe_3O_4 and Mn-, Co-, or Ni-substituted Fe_3O_4. *Phys. Rev. B: Condens. Matter Mater. Phys.* **2003**, *67*, No. 024417.
(55) Solovyev, I. V.; Dederichs, P. H.; Anisimov, V. I. Corrected atomic limit in the local-density approximation and the electronic structure of d impurities in Rb. *Phys. Rev. B* **1994**, *50*, 16861.
(56) Jonker, G. H. Analysis of the semiconducting properties of cobalt ferrite. *J. Phys. Chem. Solids* **1959**, *9*, 165.
(57) Kumar, Y.; Sharma, A.; Shirage, P. M. Impact of different morphologies of $CoFe_2O_4$ nanoparticles for tuning of structural, optical and magnetic properties. *J. Alloys Compd.* **2019**, *778*, 398−409.
(58) Li, X.; Sun, Y.; Zong, Y.; Wei, Y.; Liu, X.; Li, X.; Peng, Y.; Zheng, X. Size-effect induced cation redistribution on the magnetic properties of well-dispersed $CoFe_2O_4$ nanocrystals. *J. Alloys Compd.* **2020**, *841*, No. 155710.

https://doi.org/10.1021/acs.jpcc.3c03046
J. Phys. Chem. C 2023, 127, 17978−17986